Nano Research

Open Access

Research Article

Disentangling the role of wave function overlap, exciton–exciton interaction, carrier confinement and shape in the properties of spherical quantum wells

Marco Califano [1,2] ✉

[1] *Pollard Institute, School of Electronic and Electrical Engineering, University of Leeds, Leeds LS2 9JT, UK*
[2] *Bragg Centre for Materials Research, University of Leeds, Leeds LS2 9JT, UK*

Cite this article: *Nano Research*, **2025**, *18*, 94907162. https://doi.org/10.26599/NR.2025.94907162

ABSTRACT: There is a widespread conviction, fuelled by simple effective mass theoretical modelling, that the enhanced optical properties of quantum shells (i.e., CdS/CdSe/CdS core/shell in a shell structures) derive from a combination of relaxed carrier confinement, decreased overlap between electron and hole wave functions, reduced Coulomb interaction between photoinduced charge carriers and exciton–exciton repulsion, achieved in these nanoscopic spherical quantum wells (SQWs) by shape engineering. Confirming the origins of such properties by means of a more sophisticated theoretical framework is however important to ensure that future efforts at further improvement do not pursue the wrong strategy. Using the atomistic semiempirical pseudopotential method, we show that most of the assumptions behind such effects are incorrect, and that the origins of the peculiar optical properties of quantum shells are to be found elsewhere.

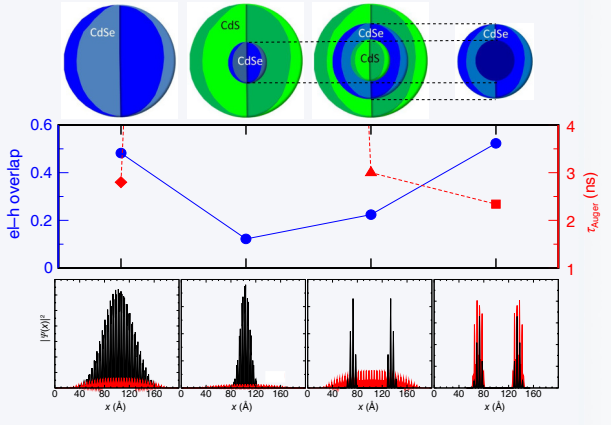

KEYWORDS: semiconductor nanocrystals, quantum shells, optical properties, electronic structure, pseudopotential method

1 Introduction

Nanoshells (NSs, also known as spherical quantum wells, SQWs) have emerged as promising geometries for a wide range of applications ranging from photovoltaics, to optoelectronics, to photoelectrochemistry [1]. In particular, the suppression of Auger recombination (AR) achieved in these nanostructures has led to blinking suppression [2], increased biexciton lifetimes [1, 3, 4], record-high (near-unity) biexciton quantum yields [3, 4], low-threshold amplified spontaneous emission [4], large modal gain [4], and spectrally narrow luminescence [4]. This is generally attributed to a synergetic combination of 4 factors: (i) relaxed carrier confinement [4, 5], (ii) reduced electron–hole (el–h) wave function overlap [1, 3], (iii) reduced Coulomb interaction [1], and (iv) exciton–exciton (X–X) repulsion [1, 3–5], although the role of (iv) is still unclear, as X–X attraction has also been reported as the origin of enhancement for both biexciton-stimulated emission and intrinsic gain coefficient, and for a reduction in the gain threshold [6].

In this work we aim to shed light on the actual effect of each of these factors on the properties of SQWs. This will provide stronger foundations onto which the optimisation of these nanostructures may be carried out further, depending on the specific target property. We will compare the properties of 4 different model structures (represented in Fig. 1), that sample realistic combinations of band-edge wave function distributions and overlaps: (a) a large CdSe core-only NC with $R = R_{tot}$; (b) a CdSe/CdS core/shell NC, with $R_{CdSe} = R_{core}$ and $R_{c/s} = R_{tot}$; (c) a CdSe NS, sandwiched between a CdS core ($R_{CdS} = R_{core}$), and a larger CdS shell ($R = R_{tot}$), with thickness $H_{CdSe} = R_{tot} - R_{core}$; (d) a hollow CdSe NS, i.e., a shell with the same dimensions as (c) but without any surrounding material. To isolate the different effects (i)–(iv) from each other and from possible strain-related effects, in all of our model structures both materials are modelled with the same lattice constant ($a_0 = a_{CdSe}$) and the same dielectric properties ($\varepsilon = \varepsilon_{CdSe}$) as CdSe. Furthermore, considering the negligible conduction band offset, and the large valence band offset, existing between CdSe and CdS [7], and according to the results of accurate *ab-initio* calculations [8], the

Received: November 1, 2024; **Revised:** November 25, 2024
Accepted: November 27, 2024

✉Address correspondence to m.califano@leeds.ac.uk

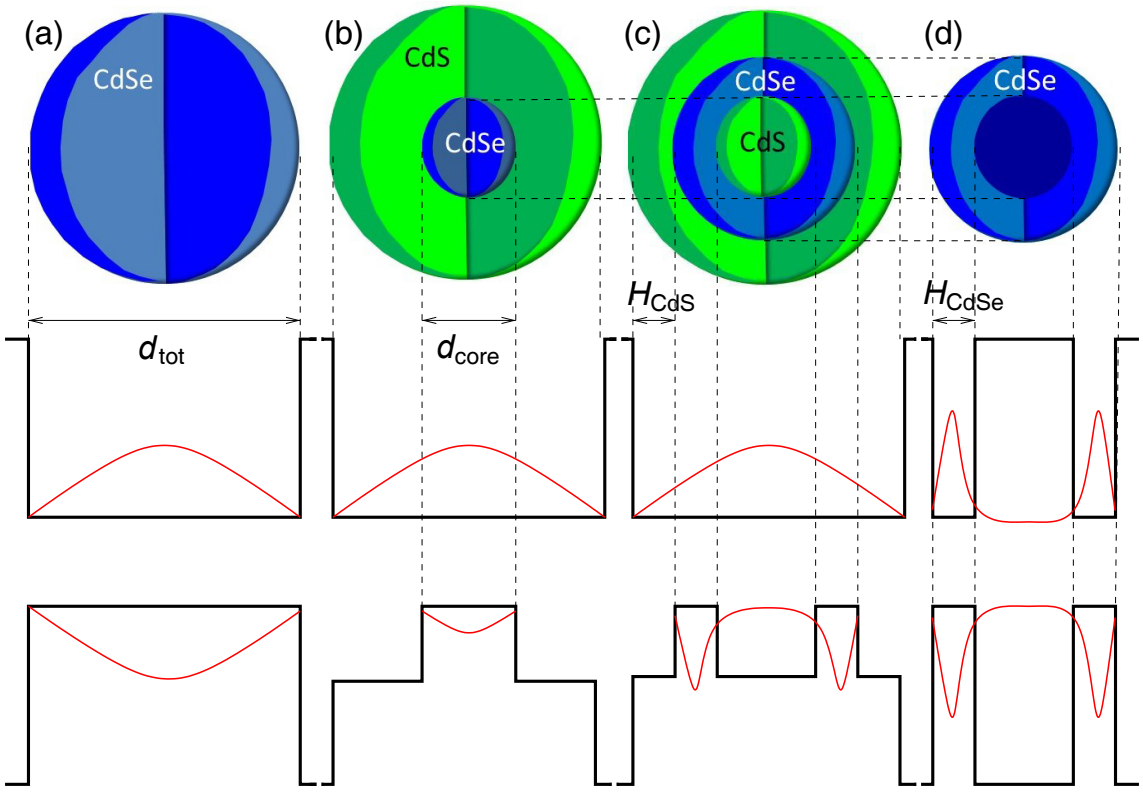

Figure 1 The nanostructures modelled in this work (with relevant dimensions) and a schematic of the corresponding band structures and relative band edge wave functions.

electron wave function in all model nanostructures is allowed to sample the whole volume, whereas the hole wave function is confined to CdSe. Indeed, Schrier and Wang [8] predicted the valence band maximum (VBM) charge density profile in SQWs to be virtually unaffected by the thickness of the CdS shell, whereas that of the conduction band minimum (CBM) to expand with increasing CdS content (either in the core or in the shell), reaching the outer radius R_{tot}. They also found the hole charge distribution to be well confined within the CdSe shell, except for the thinnest layers (0.4 and 0.8 nm), in which cases they predicted some leakage into the CdS core. Interestingly, in those same cases, the CBM charge density calculated in that work [8] exhibited a peak near or at the CdSe/CdS shell/shell interface, and one just before the CdS/CdSe core/shell interface, for any dimension sampled for both CdS core and CdS shell. This may suggest the possibility of the formation of strain-induced local minima in the conduction band structure close to the heterojunctions for thin CdSe shells, that can localise the electron. For larger and more realistic values of the CdSe shell, instead, the electron charge density was found to peak closer to the centre of the nanostructure and to extend over its whole volume.

This prediction is supported experimentally by the observation of a PL red shift upon CdS shell growth and of a slow reduction in the ratio of core to shell transient absorption bleach amplitudes as a function of the pump–probe delay [1] (all strong indications of the delocalization of the electron wave function over the entire nanoparticle volume [1]).

Charge distributions reflecting the characteristics displayed in Fig. 1 are achieved in practice in our calculations by using only one material (CdSe) in all calculations, with the localisation of both electron and hole wave functions dictated by the geometrical structure of the NC: in structures (a) and (d) both charge carriers sample the whole volume (they are both obtained by solving the Schrödinger equation for the same structure, as both NCs are made of one material—CdSe); in structures (b) and (c), instead, only the electron accesses the whole volume (the electron wave functions are the solutions of a CdSe sphere with $R = R_{tot}$—structure (a)), whereas the hole is confined to CdSe (the hole states are obtained from either a CdSe sphere with $R = R_{core}$—for structure (b)—or from a hollow shell (i.e., structure (d))—for structure (c). The supercell size is kept constant in all calculations).

A band alignment like the one in structure (c) is the one most commonly suggested to explain the properties of SQWs [1–3, 6], however that in structure (d) has also been proposed recently [5]. As mentioned above, this strategy allows us to completely remove spurious effects due to lattice and dielectric mismatch between the materials composing the nanostructure and focus exclusively on the effects of wave function overlap and spatial separation of charge carriers, of which our modelling guarantees a high level of accuracy and control. The applicability of the above model is also supported by the theoretical findings of a strong similarity between the *ab-initio* radial charge distributions obtained for a pure CdS core with $R = R_{tot}$, on the one hand, and both a CdS/CdSe/CdS SQW [8] and a CdSe/CdS core/shell NC [9], all with the same value for the total radius, on the other. The results we obtain are rather surprising, if compared to the hypotheses that have been proposed to explain the properties of NSs.

2 Results and discussion

To investigate the properties of realistic SQWs we will base our model on an experimentally synthesized core/shell in a shell structure: R_{core} = 2.25 nm, H_{CdSe} = 2 nm, H_{CdS} = 3.75 nm, and a total

radius $R_{tot} = R_{core} + H_{CdSe} + H_{CdS}$ of 8 nm [3, 4]. This structure contains over 73 × 10^3 atoms (over 80 × 10^3 if we include the passivants), the modelling of which represents a formidable task for any atomistic approach. Indeed, previous *ab-initio* calculations dealt with SQW structures with up to 18 × 10^3 atoms, with a maximum total radius of 4.3 nm (i.e, just over one half of the total radius investigated here), core radii of 1.1, 1.45 and 1.8 nm, and extremely thin CdSe wells (H_{CdSe} = 0.4–1.6 nm), and CdS shells (H_{CdS} = 0.4–1.6 nm) [8].

2.1 Charge density distribution and wave function overlap

We will start by considering the charge density distributions and the wave function overlaps of the band edges in all configurations (a)–(d) (Fig. 2), as the spatial separation of electron and hole and the ensuing low values for their overlaps have been adduced as an explanation for most of the SQWs properties [1, 3]. Figure 2 presents linescans of both band edges through the centre of the supercell along the *x* axis in all 4 structures (for structure (a) we also provide, in the inset, results for a small core-only CdSe NCs with $R = R_{core}$). A similar plot, where the wave functions have, however, also been integrated across the *yz* plane is presented in Fig. S1 in the Electronic Supplementary Material (ESM). The value of the electron–hole overlap integral (O_{el-h}) calculated over the whole nanostructure volume is reported on the top right corner of each panel. We see that the calculated profile of the wave functions displayed in Fig. 2 matches closely that schematically represented in Fig. 1, with the superimposed atomistic detail reflecting the underlying crystal lattice (as also found in *ab-initio* calculations [8]). As a consequence, we can expect the band edges' overlap to be smaller in (b) and (c) compared to (a) and (d). Due to the difference in the volume occupied by the hole (much larger in (c)) in the two structures, we may also expect that overlap in (c) may be larger than in (b).

Indeed, the smallest overlap (0.122) is found for a small-core/giant-shell nanostructure (b), followed by the SQW structure (c), with nearly twice the overlap found in (b), whereas the largest overlap is found, not surprisingly, for the hollow SQW (d), with the small core-only structure ((a)-inset), exhibiting a similar value (larger than the overlap calculated for the large core-only NC, as expected, due to the different degree of confinement in the two cores). The value we calculated for structure (b) is consistent with the experimental estimate (0.05) obtained for a CdSe/CdS core/giant-shell NC with R_{core} = 1.5 nm and a CdS shell thickness of 19 ML [10].

These results are in striking contrast to those obtained using a one-band effective-mass (EMA), particle-in-a-spherical-box approach [3], which, for structures (b) and (c) (with identical sizes to ours), predicts overlaps of 0.505 and 0.185, respectively, i.e., a larger overlap (over 4 times larger than what we calculate) for a small-core/giant-shell structure, compared to a SQW (the complete opposite to what we find).

This discrepancy is surprising, considering that a similar (EMA) approach yielded excellent agreement with the el–h overlap extracted from the measured PL lifetimes mentioned above [10]. In that case, a conduction band discontinuity of 0.1 eV between CdSe and CdS was assumed [10], compared to the value of 0.05 eV used in [3]. This smaller energy offset, however, should have resulted in a larger penetration of the electron wave function into CdS, hence in an even smaller value for the el–h overlap, considering the hole localisation in CdSe. The origins of this discrepancy remain, therefore, unclear.

We conclude this section by highlighting that core/giant-shell NCs exhibit a smaller (by a factor of nearly one half) wave function overlap than SQWs.

2.2 Exciton–exciton interaction

We next consider the exciton–exciton (X–X) interaction in these structures, and quantify it in terms of the difference $\Delta_{XX} = E_{gs}(XX) - 2E_{gs}(X)$ between the energy of the bi-exciton and twice that of the exciton (both in their ground state): negative values of Δ_{XX} indicate

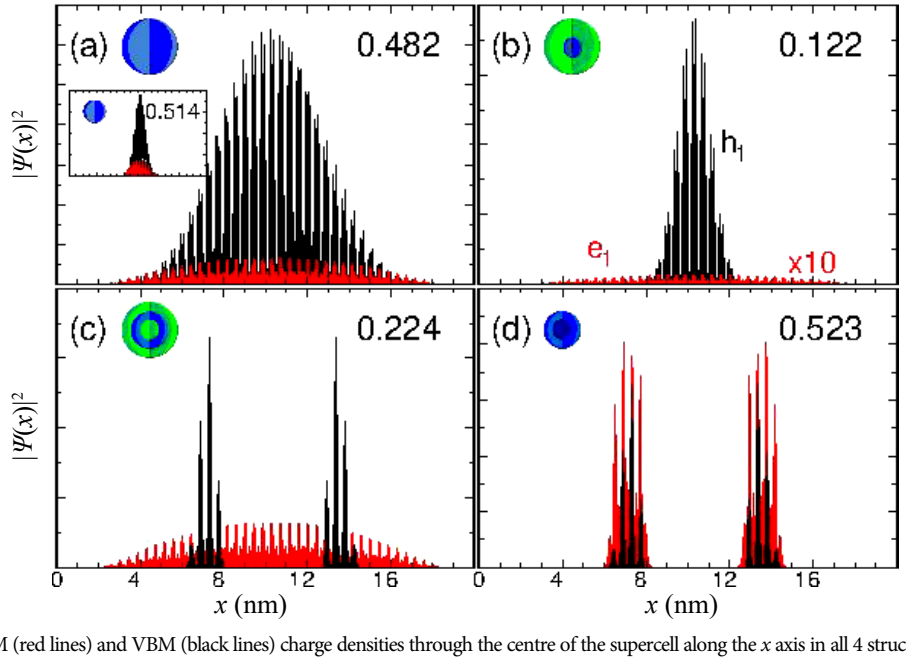

Figure 2 Linescans of CBM (red lines) and VBM (black lines) charge densities through the centre of the supercell along the *x* axis in all 4 structures (a)–(d) in Fig. 1. Also reported on the top right corner of each panel are the electron–hole overlap integrals calculated over the whole nanostructure volume. The inset in panel (a) represents the results for a small core-only CdSe NC with the same size as the core in (b) and (c).

an attractive X–X interaction, whereas positive values correspond to repulsion. X–X interaction is weakly attractive in bulk CdSe [11], but was found [12] to be enhanced (and still attractive) in core only NCs, and to follow a $1/R$ dependence, typical of Coulomb interaction, for core radii > 1.8 nm. This was attributed to the increased spatial confinement of the excitons and the reduced dielectric screening [12], although, according to Shumway et al. [13], correlation effects are mainly responsible for it.

In both SQWs [6], and CdSe/CdS core/shell NCs [14], the prevalence of one of these two regimes (i.e., attraction or repulsion) was reported to depend on the thickness of the shell, where thin shells were associated with attractive X–X interaction and thick shells with repulsive X–X interaction [6, 14]. To investigate this further, we therefore introduced an additional structure in our set (not shown in Fig. 1): a SQW with the same dimensions as that in panel (c) except for the external shell, which was chosen to be much thinner (0.5 nm, ~ 1 ML) than the one in structure (c) (3.75 nm). As the repulsive X–X interaction found in SQWs was attributed to both their quasi-type II band structure and the ensuing low value of the band edges' wave function overlap [3], in Fig. 3(a) we present Δ_{XX} for all the structures considered in this work as a function of the el–h overlap. Panel (b) of Fig. 3 shows, instead, the overlap dependence of the direct Coulomb integral

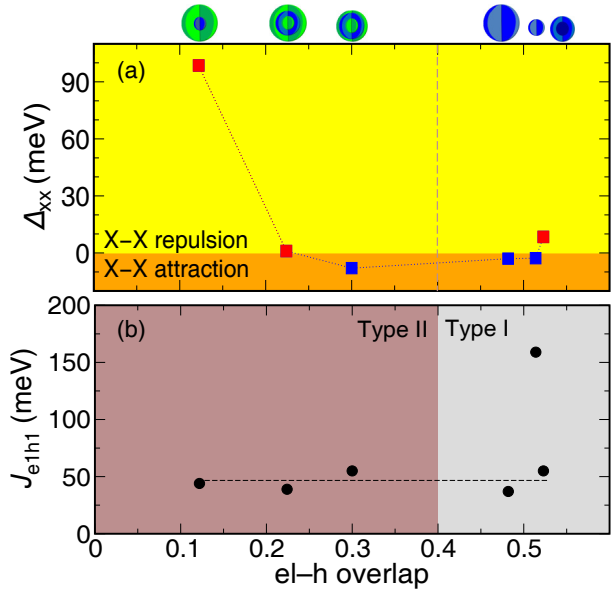

Figure 3 (a) Δ_{XX} and (b) Coulomb integral as a function of wave function overlap between the band edges for all the structures considered in this work. The yellow (orange) area in (a) indicates exciton repulsion [attraction], also highlighted by red (blue) symbols. The brown (grey) area in (b) indicates (quasi) type II (type I) band alignment. The brown dashed line in (a) is a continuation of the type I-type II boundary in (b).

$$J_{e,h} = e^2 \sum_{\sigma_h,\sigma_e} \int\int \frac{\left|\psi_h\left(\vec{r_h},\sigma_h\right)\right|^2 \left|\psi_e\left(\vec{r_e},\sigma_e\right)\right|^2}{\epsilon\left(\vec{r_h},\vec{r_e}\right)\left|\vec{r_h}-\vec{r_e}\right|} d\vec{r_h} d\vec{r_e} \quad (1)$$

where $\sigma = \uparrow\downarrow$ is the spin variable, $\psi_i\left(\vec{r_i},\sigma_i\right)$ are the single-particle wave functions solution of the Schrödinger equation, and $\epsilon\left(\vec{r_i},\vec{r_j}\right)$ is a size- and position-dependent dielectric constant [15].

Our results seem to correctly reproduce the different behaviour observed in thick- and thin-shelled SQWs, with the former exhibiting X–X repulsion and the latter attraction [6]. We want to point out, though, that X–X repulsion is only evident (and only just) from the value of Δ_{XX} (i.e., a difference between calculated ground state energies). In contrast, the BX peak in both emission and absorption spectra lies at a slightly lower energy than the X peak (calculated at ~ 1.99 eV, compared to the measured value of 1.96 eV for a SQW structure of the same dimensions [3]), in SQWs with both thick and thin shells, due to a combination of excitonic fine structure, oscillator strength associated with the different transitions, and line broadening. An additional factor that can influence X–X interaction is dielectric confinement [16], whose contribution to the total Δ_{XX} was, however, found to be small (< 30% of the direct Coulomb coupling between charges; it is negative—i.e., attractive—if the dielectric constant of the shell material is greater than that of the core, and positive for $\varepsilon_{shell} < \varepsilon_{core}$), [16] and is, by design, neglected in our modelling.

We note that, although EMA calculations predict Δ_{XX} ~ 18 meV in a SQW with the same dimensions as ours (see Fig. 5(c) in Ref. [3]), they seem to fail to predict the attractive behaviour observed in thin shell SQWs [6].

As the charge density profiles of the band edges in our SQWs are those shown in Figs. 1 (schematically) and 2, and Fig. S1 in the ESM (calculated), this result is at odds with the assumption that the exciton-exciton repulsion observed in these structures is due to the strong localization of photoinduced holes with respect to the electrons' delocalization over the nanoparticle volume [3].

The shift of the biexciton emission band with respect to the single exciton peak (i.e., $-\Delta_{XX}$), we calculate for the small and large CdSe cores ($-\Delta_{XX}$ =16 and 8 meV, respectively) are in agreement with the values predicted for NCs with R = 2.25 and 8 nm ($-\Delta_{XX}$ = 21.7 and 6.13 meV), according to the $1/R$ dependence reported by Achermann et al. [12].

In the case of a core/giant-shell NC (structure (b)), instead, the X–X repulsion is unequivocally evidenced by both the large value of Δ_{XX} and the position of the BX peak in both optical spectra laying at a higher energy than that of X, in agreement with experimental observation [14, 17].

From inspection of Fig. 3(a) it is also clear that, although, quasi-type II band alignment and low values of the el–h overlap may lead to some degree of X–X repulsion, type I structures exhibiting large el–h overlaps (hollow SQWs, structure (d) in Fig. 1), can exhibit larger X–X repulsion than conventional SQWs. As hollow SQWs have no shell, our results question the assumption that the origin of X–X repulsion in experimental SQWs is simply due to a combination of quasi-type II band structure, low el–h overlap and a thick shell.

Interestingly, Fig. 3 also shows the Coulomb interaction (whose strength is often invoked to explain excitonic effects/carrier dynamics in nanostructures), to be insensitive to the type of band alignment and to the magnitude of the el–h overlap, and to depend, instead, more on the strength of confinement experienced by the charge carriers, in agreement with the results of previous *ab-initio* calculations [8], which found $J_{e,h}$ to depend more sensitively on the spatial distribution of the electron charge density.

We note that our calculated Stokes shift in a SQW is of the order of a few meV, and much smaller than the experimental value reported by Cassidy et al. [3] (~ 60 meV), which, interestingly, matches nearly exactly the energetic separation between the peaks attributed to X and XX in their amplified spontaneous emission (ASE) spectrum [3].

2.3 Radiative lifetimes

One property we find to be strongly dependent on the el–h overlap is the radiative recombination time of both BX and X (Fig. 4), which can vary by nearly 2 orders of magnitude, from hundreds [thousands] of ns in a core/giant-shell NC (the structure with the longest predicted lifetimes among those considered here), to a few [tens of] ns for the bi-exciton [exciton] lifetimes calculated in the case of a hollow SQW or a core-only NC of any size, respectively. We find this dependence to follow a power law

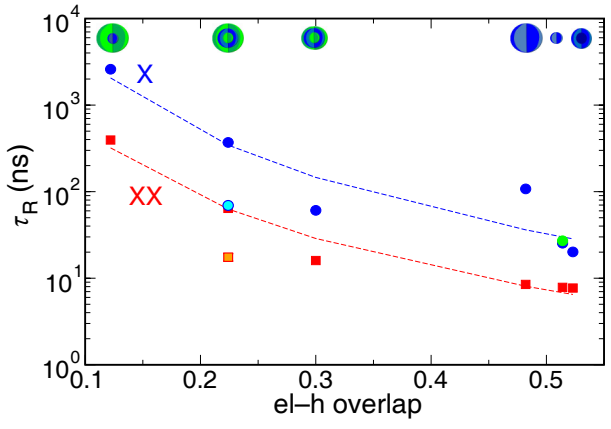

Figure 4 Calculated single- (X, blue circles and line) and bi-exciton (XX, red squares and line) room temperature radiative lifetimes as a function of wave function overlap between the band edges for all the structures considered in this work (dispersed in toluene). Available experimental results for a CdS/CdSe/CdS SQW of the same size as ours (cyan circle and orange square) [3] and a CdSe core-only NCs with the same emission energy as ours (green circle) [18], are presented for comparison. The dashed lines are the fitted power laws (see text for details).

$$\tau_R^Z(O_{\mathrm{el-h}}) = \alpha_Z O_{\mathrm{el-h}}^{-\beta_Z} \quad (2)$$

over the overlap range considered, where Z = X, XX, α_X = 4.8, α_{XX} = 1.25, β_X = 2.94, and β_{XX} = 2.7. This implies a ~ cubic dependence on the overlap for the radiative rates.

The values of τ_R^X and τ_R^{XX} we calculate at room temperature for our thick-shell SQW (371 and 64 ns, respectively) are about a factor of 5 and 4, respectively, larger than the estimates obtained experimentally for SQW samples of the same sizes (69.2 and 15.8–19.2 ns, respectively, cyan circle and orange square in Fig. 4) [3], where the latter values were derived from the measured exciton and biexciton lifetimes τ_R^X and τ_R^{XX} according to $\tau_R^Z = \tau^Z/\mathrm{QY}(Z)$ (where QY(Z) is the experimental quantum yield). The agreement with experiment is however excellent for our thin-shell SQW (i.e., the lifetimes relative to an el–h overlap of 0.3, in Fig. 4), for which the calculated τ_R^X and τ_R^{XX} are 60.9 and 16 ns, respectively. This may suggest a very limited electron delocalisation into the shell in the experimental sample. Indeed, this behaviour is consistent with the findings, by Garcia-Santamaria et al. [10], of a saturation in the 1S transition energies in CdSe/CdS core/giant-shell NCs, occurring when the total NC radius exceeded ~ 4 nm (in our SQW R_{core} + H_{CdSe} = 4.2 nm), which was interpreted as an indication that in these systems the effective exciton radius does not increase with the shell thickness when R_{tot} > 4 nm. Alternatively, such an increase in electron confinement could result from the formation of a potential well at, or close to, the CdSe/CdS heterojunction, possibly originating from lattice strain or some other interface effect (as discussed above [8]), or from a strong attraction by the CdSe-localized hole. A similar effect was, indeed, reported in the case of CdSe/CdS core/giant-shell NCs [19], where the observed gradual reduction of the PL red shift with increasing CdS shell thickness was attributed [19] to the reduced exciton spread due to the attractive Coulomb potential of the core-localized hole.

In spite of the agreement above, however, we note that the radiative times calculated for CdSe/CdS heterostructure NCs are not supposed to be strictly compared with experimental data, since, as we explained in the introduction, our model structures are intended as samples of different combinations of electron and hole confinement profiles, charge distributions, and wave function overlaps, and they deliberately neglect to differentiate between the material properties of CdS and CdSe (such as their lattice constants and band structures). As such, they can only represent a rough approximation to actual heteronanostructures. Nevertheless, their relative comparison is meaningful, as it captures the effects of the parameters we focused on in this work (in this case, the el–h overlap), decoupled from the influence of heterostructure-specific causes. The radiative times calculated for pure CdSe [20, 21] and other monomaterial NCs [22, 23] have, instead, proven to be very accurate.

Indeed, the radiative recombination lifetime we calculate for a CdSe core-only NC with R = 2.25 nm, and emission at 2.025 eV (25.3 ns), is also in excellent agreement with that measured for a CdSe dot emitting at 2.0 eV (27.03 ns, green circle in Fig. 4) by Van Driel et al. [18].

2.4 Auger recombination

Figure 5 displays the AR times (right-hand y axis) and the calculated el–h overlaps (left-hand y axis) for all 4 structures considered (where the filled symbols represent the results of the present work and the empty symbols experimental data/estimates [3, 10, 24, 25]). Owing to the large size of the nanostructures considered here (R_{tot} = 8 nm), the density of states at the energies relevant for AR transitions (i.e., a band gap away from the band edges) is prohibitively large. This, unfortunately, prevented us from

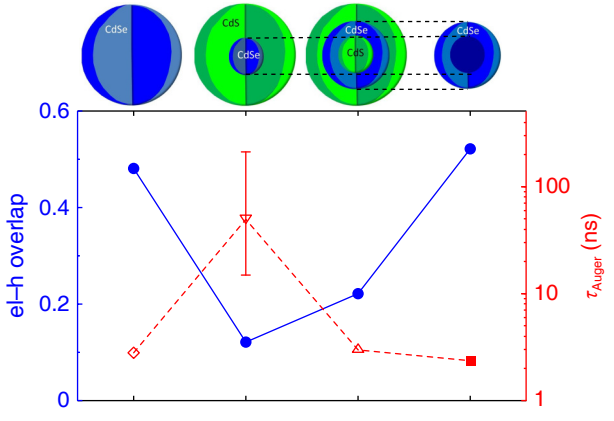

Figure 5 AR lifetimes (red symbols, right-hand y axis) and calculated el-h overlaps (blue circles, left-hand y axis) for all 4 structures considered in this work. The AR time we calculate for the hollow CdSe SQW shown as structure (d) in Fig. 1 is presented as a solid square. Also displayed for comparison are: the measured AR time for a CdS/CdSe/CdS SQW of identical size as our structure (c) (triangle up) [3], the experimental estimates (15–210 ns [24] and 60–120 ns [10]) obtained for CdSe/CdS core/giant-shell structures with similar total radius to our CdSe/CdS structure and a slightly smaller core (R_{core} = 1.5 nm, triangle down), and the AR time for a core-only CdSe NC with the same total radius (structure (a), diamond), extrapolated from the AR times measured for smaller NCs, based on the volume dependence found in Ref. [25]. The lines are a guide to the eye.

carrying out a reliable calculation of AR times. In the case of a hollow CdSe shell (i.e., structure (d) in Fig. 1), however, we succeeded in identifying an energy window of a few meV around the resonant energy for both electron and hole excitation, which allowed us a better accuracy in the calculation. Furthermore, considering the uniform composition of the shell and its material (CdSe), and our track record in calculating AR times for pure CdSe NCs [26] we expect our results to be quite accurate [26] in this case. The AR time we calculate for this structure—2.34 ns—is virtually identical to the experimental value obtained for a full SQW (i.e., structure (c) in Fig. 1)—3 ns [3]. Considering that structure (d) has a volume nearly 10 times smaller than structure (c), and an el–h overlap over twice as large, this result represents compelling evidence that large exciton volume and small el–h overlap cannot be the origin of the AR suppression observed in SQWs. Furthermore, we find the negative trion AR in structure (d) to be more efficient than the positive trion recombination, with τ_{X-} nearly twice as fast as τ_{X+}. This result is in clear contrast with the hypothesis [6] of the delocalization of the hole wave function from the center of the SQW being responsible for the reduced Auger interaction of the biexcitons, due to the latter being dominated by positive trion recombination.

We want to emphasise once more that these results assume the band edges' charge density profiles shown in Figs. 1 (schematically) and 2, and Fig. S1 in the ESM (calculated), which may not represent the actual profiles in the experimental samples, as was discussed above. Our results again suggest a smaller extent for the electron delocalization into CdS in experimental samples than currently assumed, and are consistent with the experimental observations [10], of a saturation in the 1S transition energies in CdSe/CdS core/giant-shell NCs, occurring when the total NC radius exceeded ~ 4 nm mentioned above, hinting at the possibility that in these systems the effective exciton radius does not increase with the shell thickness above $R = 4$ nm.

3 Conclusions

By deliberately neglecting to differentiate between the material properties of CdS and CdSe, we focused specifically on the aspects that have been suggested as possible origins of the peculiar properties of spherical quantum wells: (i) relaxed carrier confinement, (ii) reduced electron–hole wave function overlap, (iii) reduced Coulomb interaction, and (iv) exciton–exciton repulsion. We compared the properties of 6 different model structures with dimensions taken from experimental samples and containing a staggering number of atoms (80×10^3) for an atomistic approach, that sample realistic combinations of band alignments, band-edge wave function distributions and el–h overlaps ((a) a small and a large CdSe core-only NC; (b) a CdSe/CdS core/shell NC; (c) a CdSe NS, sandwiched between a CdS core and a CdS shell with two different thicknesses; (d) a hollow CdSe NS). We found that: (1) core/giant-shell NCs exhibit a smaller (by a factor of nearly one half) wave function overlap than SQWs of the same total volume, in striking contrast to the predictions of a one-band effective-mass, particle-in-a-spherical-box approach, which is commonly being relied on to explain the properties of experimental SQWs; (2) despite our results correctly reproducing the different X–X interaction observed in thick- and thin-shelled SQWs (X–X repulsion and attraction, respectively), X–X repulsion is only evident when considering ground state energies, whereas the calculated BX peak in both emission and absorption spectra lies at a slightly lower energy than the X peak in SQWs with both thick and thin shells; (3) although, quasi-type II band alignment and low values of the el–h overlap may lead to some degree of X–X repulsion, type I structures exhibiting large el–h overlaps (hollow SQWs), can exhibit larger X–X repulsion than conventional SQWs. As hollow SQWs have no outer shell, this result questions the assumption that the origin of X–X repulsion in experimental SQWs is simply due to a combination of quasi-type II band structure, low el–h overlap and a thick shell; (4) the Coulomb interaction (whose strength is often invoked to explain excitonic effects and carrier dynamics in nanostructures), is insensitive to the type of band alignment and to the magnitude of the el–h overlap, and depends, instead, more on the strength of confinement experienced by the charge carriers; (5) the calculated AR time for a hollow SQW is virtually identical to the experimental value obtained for a full SQW: considering that the former has a volume nearly 10 times smaller than the latter structure, and an el–h overlap over twice as large, this result refutes the hypothesis that large exciton volume and small el–h overlap are at the origin of the AR suppression observed in SQWs.

In summary we have provided ample and compelling evidence that the assumptions made so far regarding the factors responsible for the enhanced properties of SQWs are inconsistent with the results of a sophisticated atomistic theory and that, therefore, the origin of such properties needs to be sought elsewhere. Our results also strongly suggest the charge density distribution in experimental SQWs to be very different from what is commonly assumed (i.e., the hole confined to the CdSe shell and the electron free to sample the whole structure volume). As these charge distribution profiles are also supported by the results of accurate density function theory (DFT) calculations, based on small, model SQWs with uniform material composition within each layer (i.e., with sharp interfaces between CdS and CdSe), the large discrepancy between experiment and theory shown here hints at the possibility of alternative scenarios regarding the actual composition profile and crystal structure of experimental SQW samples, such as the presence of stacking faults, strongly strained layers, alloyed or composition-graded interfaces.

4 Method

The NCs considered in this work have a bulk-like crystal structure and are modelled in their wurtzite phase. The unsaturated bonds at the NC surface are passivated by pseudo-hydrogenic, short-range potentials with Gaussian form [27]. This procedure ensures an ideal passivation, allowing us to focus on the intrinsic properties of these nanostructures.

The single-particle energies ε_i and wave functions ψ_i are obtained by solving the single-particle Schrödinger equation

$$\left[-\frac{\hbar^2}{2m}\nabla^2 + V\left(\vec{r}\right)\right]\psi_i\left(\vec{r}\right) = \varepsilon_i\psi_i\left(\vec{r}\right) \tag{3}$$

using the plane-wave semiempirical pseudopotential method (SEPM) described in [28], where the total potential is expressed as

$$V\left(\vec{r}\right) = V_{ps}\left(\vec{r}\right) + V_{nl} \tag{4}$$

In Eq. (4) V_{nl} accounts for the nonlocal part of the potential and includes the spin-orbit (SO) coupling, and the microscopic pseudopotential of the system $V_{ps}(r)$ is obtained as a superposition of screened atomic potentials,

$$V_{\mathrm{ps}}\left(\vec{r}\right)=\sum_{i,\alpha} v_{\alpha}\left(\vec{r}-\vec{R}_{i,\alpha}\right) \tag{5}$$

where $v_{\alpha}\left(\vec{r}-\vec{R}_{i,\alpha}\right)$ is the atomic potential for an atom of type α located at the position $\vec{R}_{i,\alpha}$. The atomic pseudopotentials are derived from bulk local-density approximation (LDA) calculations and are adjusted to remove LDA errors in band gaps and effective masses. Polarization effects are neglected, since, as expected from electrostatic arguments [29], and confirmed by tight-binding GW calculations [30], the polarization self-energy almost exactly cancels out the Coulomb polarization term for small dielectric mismatches between the two materials composing the NC [31].

Due to the large number of atoms involved, Eq. (3) is solved using the folded spectrum method [32, 33], which allows one to calculate exactly only selected eigenstates of the Schrödinger equation around an arbitrary reference energy $\varepsilon_{\mathrm{ref}}$. In this approach Eq. (3) is replaced by

$$\left[-\frac{\hbar^2}{2m}\nabla^2+V\left(\vec{r}\right)-\varepsilon_{\mathrm{ref}}\right]^2\psi_i\left(\vec{r}\right)=\left(\varepsilon_i-\varepsilon_{\mathrm{ref}}\right)^2\psi_i\left(\vec{r}\right) \tag{6}$$

whose ground state coincides with the solutions of Eq. (3) with energy closest to $\varepsilon_{\mathrm{ref}}$. The band edge states of the nanocrystals can be obtained by choosing $\varepsilon_{\mathrm{ref}}$ inside the band gap. The minimization procedure is carried out in a supercell with periodic boundary conditions with a plane-wave basis set using a preconditioned conjugate-gradients algorithm.

Excitonic effects are accounted for via a configuration interaction (CI) scheme, including Coulomb and exchange interactions [15], where the excitonic wave functions Ψ_i are expanded in terms of single-substitution Slater determinants $\Phi_{v,c}$ constructed using the single-particle wave functions as

$$\Psi^{(i)}=\sum_{v=1}^{N_v}\sum_{c=1}^{N_c}C_{v,c}^{(i)}\Phi_{v,c} \tag{7}$$

where N_v and N_c are the number of valence and conduction states included in the expansion. Up to 30 valence states and 17 conduction states are used in this expansion, corresponding to CI basis sets of 2040 configurations for X and of nearly 10^6 for BX.

The matrix elements of the many-particle Hamiltonian $\mathcal{H}$ in the basis set $\Phi_{v,c}$ are calculated as [15]

$$\mathcal{H}_{vc,v'c'}\equiv\left\langle\Phi_{v,c}\left|\mathcal{H}\right|\Phi_{v',c'}\right\rangle=\left(\varepsilon_c-\varepsilon_v\right)\delta_{v,v'}\delta_{c,c'}-J_{vc,v'c'}+K_{vc,v'c'} \tag{8}$$

where J and K are the Coulomb direct and exchange integrals, respectively

$$J_{vc,v'c'}=e^2\sum_{\sigma_1,\sigma_2}\int\int \frac{\psi_{v'}^{*}\left(\vec{r}_1,\sigma_1\right)\psi_c^{*}\left(\vec{r}_2,\sigma_2\right)\psi_v\left(\vec{r}_1,\sigma_1\right)\psi_{c'}\left(\vec{r}_2,\sigma_2\right)}{\bar{\epsilon}\left(\vec{r}_1,\vec{r}_2\right)\left|\vec{r}_1-\vec{r}_2\right|}\mathrm{d}\vec{r}_1\mathrm{d}\vec{r}_2 \tag{9}$$

$$K_{vc,v'c'}=e^2\sum_{\sigma_1,\sigma_2}\int\int \frac{\psi_{v'}^{*}\left(\vec{r}_1,\sigma_1\right)\psi_c^{*}\left(\vec{r}_2,\sigma_2\right)\psi_{c'}\left(\vec{r}_1,\sigma_1\right)\psi_v\left(\vec{r}_2,\sigma_2\right)}{\bar{\epsilon}\left(\vec{r}_1,\vec{r}_2\right)\left|\vec{r}_1-\vec{r}_2\right|}\mathrm{d}\vec{r}_1\mathrm{d}\vec{r}_2 \tag{10}$$

and $\sigma=\uparrow\downarrow$ is the spin variable. The screening of the electron-hole interaction, caused by the polarization of the medium, is described phenomenologically by the microscopic, position- and size-dependent dielectric constant $\bar{\epsilon}\left(\vec{r}_1,\vec{r}_2\right)$ whose electronic (i.e., high-frequency) and ionic (i.e., low-frequency) contributions are approximated by the Thomas-Fermi model by Resta [34] and the polaronic model of Haken [15], respectively (further details can be found in Ref. [15]).

This well-benchmarked and accurate method has been used in the past to successfully model a wide range of experimental features, including the size-dependent conduction and valence band edge energies in spherical nanocrystals of different materials [35], the charge dynamics in CdSe [36, 37] and CdTe [37, 38] nanostructures, the exciton dynamics in CdTe [39] and InSb [22] colloidal dots, the optical properties of excitons, biexcitons and trions in CdSe NCs [20], the Auger rates in CdSe nanocrystals [26], and the electronic structure and optical properties of CdSe [40], CdTe [41] and CdTe/CdSe [42] tetrapods, and of In-based and Cd-based tetrahedral NCs [23].

The room temperature lifetimes are calculated as

$$\frac{1}{\tau_R\left(T\right)}=\frac{\sum_i\left(1/\tau_i\right)\mathrm{e}^{-\Delta E_i/k_{\mathrm{B}}T}}{\sum_i\mathrm{e}^{-\Delta E_i/k_{\mathrm{B}}T}} \tag{11}$$

where we assume Boltzmann occupation of high energy excitonic levels. τ_i is the radiative lifetime for the transition from state Ψ_i to the ground state, obtained as [43]

$$\frac{1}{\tau_i}=\frac{4nF^2\alpha\omega_i^3}{3c^2}\left|M_i\right|^2 \tag{12}$$

where n is the refractive index of the medium surrounding the NC (here we assume n = 1.496 corresponding to toluene), $F=3\varepsilon/(\varepsilon_{\mathrm{dot}}+2\varepsilon)$ is the screening factor, $\varepsilon=n^2$, $\varepsilon_{\mathrm{dot}}$ is the size-dependent dielectric constant of the quantum dot [15], α is the fine structure constant, ω_i is the frequency of the emitted photon, c is the speed of light, and

$$\left|M_i\right|=\sum\nolimits_{\mathrm{h,e}}C_{\mathrm{h,e}}^{(i)}\left\langle\psi_{\mathrm{h}}\left|\vec{r}\right|\psi_{\mathrm{e}}\right\rangle \tag{13}$$

is the CI dipole moment [15].

Auger recombination rates W_i are calculated according to a consolidated procedure [26,44] as

$$W_i=\frac{\Gamma}{\hbar}\sum\nolimits_n\frac{\left|\left\langle i\left|\Delta H\right|f_n\right\rangle\right|^2}{\left(E_{f_n}-E_i\right)^2+\left(\Gamma/2\right)^2} \tag{14}$$

where $|i\rangle$ and $|f_n\rangle$ are the initial and final Auger states, E_i and E_{fn} their corresponding energies, ΔH is the Coulomb interaction, and the sum is over multiple final states n (including spin), assumed to have a finite lifetime $\hbar\Gamma$ (here Γ = 10 meV is used). The Coulomb interaction ΔH is screened assuming bulk-like dielectric constants within the NC ($\epsilon_{\mathrm{core}}=\epsilon_{\mathrm{bulk(core)}}$, $\epsilon_{\mathrm{shell1}}=\epsilon_{\mathrm{bulk(shell1)}}$, $\epsilon_{\mathrm{shell2}}=\epsilon_{\mathrm{bulk(shell2)}}$, and the solvent dielectric constant outside it ($\epsilon_{\mathrm{out}}=\epsilon_{\mathrm{solvent}}$), the different regions connected by a function varying smoothly between the two dielectric constants across the interface [26, 44].

Electronic Supplementary Material: Supplementary material (*yz*-integrated linescans of the band edges' charge densities through the centre of the supercell along the *x* axis in all 4 structures) is available in the online version of this article at https://doi.org/10.26599/NR.2025.94907162.

Data availability

All data needed to support the conclusions in the paper are presented in the manuscript and the Electronic Supplementary

Material. Additional data related to this paper may be requested from the corresponding author upon request.

Acknowledgements

This work was undertaken on ARC3, part of the High-Performance Computing facilities at the University of Leeds, UK. M.C. gratefully acknowledges financial support from the School of Electronic & Electrical Engineering, University of Leeds.

Declaration of competing interest

The author reports no conflict of interests in this work.

Author contribution statement

The author confirms sole responsibility for the following: study conception and design, calculations, analysis and interpretation of results, and manuscript preparation.

Use of AI statement

None.

References

[1] Kholmicheva, N.; Budkina, D. S.; Cassidy, J.; Porotnikov, D.; Harankahage, D.; Boddy, A.; Galindo, M.; Khon, D.; Tarnovsky, A. N.; Zamkov, M. Sustained biexciton populations in nanoshell quantum dots. *ACS Photonics* **2019**, *6*, 1041–1050.

[2] Jeong, B. G.; Park, Y. S.; Chang, J. H.; Cho, I.; Kim, J. K.; Kim, H.; Char, K.; Cho, J.; Klimov, V. I.; Park, P. et al. Colloidal spherical quantum wells with near-unity photoluminescence quantum yield and suppressed blinking. *ACS Nano* **2016**, *10*, 9297–9305.

[3] Cassidy, J.; Diroll, B. T.; Mondal, N.; Berkinsky, D. B.; Zhao, K. H.; Harankahage, D.; Porotnikov, D.; Gately, R.; Khon, D.; Proppe, A. et al. Quantum shells boost the optical gain of lasing media. *ACS Nano* **2022**, *16*, 3017–3026.

[4] Marder, A. A.; Cassidy, J.; Harankahage, D.; Beavon, J.; Gutiérrez-Arzaluz, L.; Mohammed, O. F.; Mishra, A.; Adams, A. C.; Slinker, J. D.; Hu, Z. J. et al. CdS/CdSe/CdS spherical quantum wells with near-unity biexciton quantum yield for light-emitting-device applications. *ACS Materials Lett.* **2023**, *5*, 1411–1419.

[5] Harankahage, D.; Cassidy, J.; Beavon, J.; Huang, J. M.; Brown, N.; Berkinsky, D. B.; Marder, A.; Kayira, B.; Montemurri, M.; Anzenbacher, P. et al. Quantum shell in a shell: Engineering colloidal nanocrystals for a high-intensity excitation regime. *J. Am. Chem. Soc.* **2023**, *145*, 13326–13334.

[6] Nagamine, G.; Jeong, B. G.; Ferreira, T. A. C.; Chang, J. H.; Park, K.; Lee, D. C.; Bae, W. K.; Padilha, L. A. Efficient optical gain in spherical quantum wells enabled by engineering biexciton interactions. *ACS Photonics* **2020**, *7*, 2252–2264.

[7] Li, Y. H.; Walsh, A.; Yin, W. J.; Yang, J. H.; Li, J.; Da Silva, J. L. F.; Gong, X. G.; Wei, S. H. Revised *ab initio* natural band offsets of all group IV, II-VI, and III-V semiconductors. *Appl. Phys. Lett.* **2009**, *94*, 212109.

[8] Schrier, J.; Wang, L. W. Electronic structure of nanocrystal quantum-dot quantum wells. *Phys. Rev. B* **2006**, *73*, 245332.

[9] Li, J. B.; Wang, L. W. First principle study of core/shell structure quantum dots. *Appl. Phys. Lett.* **2004**, *84*, 3648–3650.

[10] Garcia-Santamaría, F.; Brovelli, S.; Viswanatha, R.; Hollingsworth, J. A.; Htoon, H.; Crooker, S. A.; Klimov, V. I. Breakdown of volume scaling in auger recombination in CdSe/CdS heteronanocrystals: The role of the core–shell interface. *Nano Lett.* **2011**, *11*, 687–693.

[11] Shionoya, S.; Saito, H.; Hanamura, E.; Akimoto, O. Anisotropic excitonic molecules in CdS and CdSe. *Solid State Commun.* **1973**, *12*, 223–226.

[12] Achermann, M.; Hollingsworth, J. A.; Klimov, V. I. Multiexcitons confined within a subexcitonic volume: Spectroscopic and dynamical signatures of neutral and charged biexcitons in ultrasmall semiconductor nanocrystals. *Phys. Rev. B* **2003**, *68*, 245302.

[13] Shumway, J.; Franceschetti, A.; Zunger, A. Correlation versus mean-field contributions to excitons, multiexcitons, and charging energies in semiconductor quantum dots. *Phys. Rev. B* **2001**, *63*, 155316.

[14] Bisschop, S.; Geiregat, P.; Aubert, T.; Hens, Z. The impact of core/shell sizes on the optical gain characteristics of CdSe/CdS quantum dots. *ACS Nano* **2018**, *12*, 9011–9021.

[15] Franceschetti, A.; Fu, H.; Wang, L. W.; Zunger, A. Many-body pseudopotential theory of excitons in InP and CdSe quantum dots. *Phys. Rev. B* **1999**, *60*, 1819–1829.

[16] Piryatinski, A.; Ivanov, S. A.; Tretiak, S.; Klimov, V. I. Effect of quantum and dielectric confinement on the exciton–exciton interaction energy in type II core/shell semiconductor nanocrystals. *Nano Lett.* **2007**, *7*, 108–115.

[17] Klimov, V. I.; Ivanov, S. A.; Nanda, J.; Achermann, M.; Bezel, I.; McGuire, J. A.; Piryatinski, A. Single-exciton optical gain in semiconductor nanocrystals. *Nature* **2007**, *447*, 441–446.

[18] van Driel, A. F.; Allan, G.; Delerue, C.; Lodahl, P.; Vos, W. L.; Vanmaekelbergh, D. Frequency-dependent spontaneous emission rate from CdSe and CdTe nanocrystals: Influence of dark states. *Phys. Rev. Lett.* **2005**, *95*, 236804.

[19] Christodoulou, S.; Vaccaro, G.; Pinchetti, V.; De Donato, F.; Grim, J. Q.; Casu, A.; Genovese, A.; Vicidomini, G.; Diaspro, A.; Brovelli, S. et al. Synthesis of highly luminescent wurtzite CdSe/CdS giant-shell nanocrystals using a fast continuous injection route. *J. Mater. Chem. C* **2014**, *2*, 3439–3447.

[20] Califano, M.; Franceschetti, A.; Zunger, A. Lifetime and polarization of the radiative decay of excitons, biexcitons, and trions in CdSe nanocrystal quantum dots. *Phys. Rev. B* **2007**, *75*, 115401.

[21] Califano, M.; Franceschetti, A.; Zunger, A. Temperature dependence of excitonic radiative decay in CdSe quantum dots: The role of surface hole traps. *Nano Lett.* **2005**, *5*, 2360–2364.

[22] Sills, A.; Harrison, P.; Califano, M. Exciton dynamics in InSb colloidal quantum dots. *J. Phys. Chem. Lett.* **2016**, *7*, 31–35.

[23] Califano, M. Tetrahedral vs spherical nanocrystals: Does the shape really matter. *Chem. Mater.* **2024**, *36*, 1162–1171.

[24] García-Santamaría, F.; Chen, Y. F.; Vela, J.; Schaller, R. D.; Hollingsworth, J. A.; Klimov, V. I. Suppressed auger recombination in "giant" nanocrystals boosts optical gain performance. *Nano Lett.* **2009**, *9*, 3482–3488.

[25] Robel, I.; Gresback, R.; Kortshagen, U.; Schaller, R. D.; Klimov, V. I. Universal size-dependent trend in auger recombination in direct-gap and indirect-gap semiconductor nanocrystals. *Phys. Rev. Lett.* **2009**, *102*, 177404.

[26] Wang, L. W.; Califano, M.; Zunger, A.; Franceschetti, A. Pseudopotential theory of auger processes in CdSe quantum dots. *Phys. Rev. Lett.* **2003**, *91*, 056404.

[27] Graf, P. A.; Kim, K.; Jones, W. B.; Wang, L. W. Surface passivation optimization using DIRECT. *J. Comput. Phys.* **2007**, *224*, 824–835.

[28] Wang, L. W.; Zunger, A. Local-density-derived semiempirical pseudopotentials. *Phys. Rev. B* **1995**, *51*, 17398–17416.

[29] Bányai, L.; Gilliot, P.; Hu, Y. Z.; Koch, S. W. Surface polarization instabilities of electron–hole pairs in semiconductor quantum dots. *Phys. Rev. B* **1992**, *45*, 14136–14142.

[30] Delerue, C.; Lannoo, M.; Allan, G. Excitonic and quasiparticle gaps in Si nanocrystals. *Phys. Rev. Lett.* **2000**, *84*, 2457–2460.

[31] Karpulevich, A.; Bui, H.; Wang, Z.; Hapke, S.; Palencia Ramírez, C.; Weller, H.; Bester, G. Dielectric response function for colloidal semiconductor quantum dots. *J. Chem. Phys.* **2019**, *151*, 224103.

[32] Wang, L. W.; Zunger, A. Solving Schrödinger's equation around a

desired energy: Application to silicon quantum dots. *J. Chem. Phys.* **1994**, *100*, 2394–2397.
[33] Wang, L. W.; Zunger, A. Electronic structure pseudopotential calculations of large (~ 1000 atoms) Si quantum dots. *J. Phys. Chem.* **1994**, *98*, 2158–2165.
[34] Resta, R. Thomas-fermi dielectric screening in semiconductors. *Phys. Rev. B* **1977**, *16*, 2717–2722.
[35] Jasieniak, J.; Califano, M.; Watkins, S. E. Size-dependent valence and conduction band-edge energies of semiconductor nanocrystals. *ACS Nano* **2011**, *5*, 5888–5902.
[36] Zhu, H. M.; Yang, Y.; Hyeon-Deuk, K.; Califano, M.; Song, N. Y.; Wang, Y. W.; Zhang, W. Q.; Prezhdo, O. V.; Lian, T. Q. Auger-assisted electron transfer from photoexcited semiconductor quantum dots. *Nano Lett.* **2014**, *14*, 1263–1269.
[37] Califano, M. Charge dynamics in quantum-dot-acceptor complexes in the presence of confining and deconfining ligands. *J. Phys. Chem. Lett.* **2020**, *11*, 280–285.
[38] Harvie, A. J.; Smith, C. T.; Ahumada-Lazo, R.; Jeuken, L. J. C.; Califano, M.; Bon, R. S.; Hardman, S. J. O.; Binks, D. J.; Critchley, K. Ultrafast trap state-mediated electron transfer for quantum dot redox sensing. *J. Phys. Chem. C* **2018**, *122*, 10173–10180.
[39] Califano, M. Origins of photoluminescence decay kinetics in CdTe colloidal quantum dots. *ACS Nano* **2015**, *9*, 2960–2967.
[40] Li, J. B.; Wang, L. W. Shape effects on electronic states of nanocrystals. *Nano Lett.* **2003**, *3*, 1357–1363.
[41] Zhou, Y.; Califano, M. Decoupling radiative and auger processes in semiconductor nanocrystals by shape engineering. *J. Phys. Chem. Lett.* **2021**, *12*, 9155–9161.
[42] Califano, M.; Zhou, Y. Inverse-designed semiconductor nanocatalysts for targeted CO_2 reduction in water. *Nanoscale* **2021**, *13*, 10024–10034.
[43] Dexter, D. L. *Solid State Physics*; Academic Press Inc.: New York, 1958; pp 358–361.
[44] Califano, M. Suppression of auger recombination in nanocrystals via ligand-assisted wave function engineering in reciprocal space. *J. Phys. Chem. Lett.* **2018**, *9*, 2098–2104.